Surrogate Modeling and Optimization of a Combustor with an Interdigitated Flushwall Injector

Rajiv R. Shenoy,[†] Tomasz G. Drozda,[‡] Robert A. Baurle,[‡] and Peter A. Parker,[§]
NASA Langley Research Center, Hampton, VA 23681

ABSTRACT

Design and Analysis of Computer Experiments (DACE) methods are applied and used to perform surrogate modeling and optimization of a simplified combustor flowpath with an interdigitated flushwall injector. The objectives of the optimization are the thrust potential and combustion efficiency, which are evaluated across a range of flight Mach numbers, duct heights, spanwise spacings, and injection angles. The focus of this work is to highlight the application of a sequential learning approach, in order to learn about the responses of the objective functions over the design space and to identify local regions of interest for further analysis. This approach is contrasted to a previous effort where only a single sampling set was used to fit surrogate models and perform optimization. The optimal solutions resulting from the previous and present approaches are different, due to surrogate model-guided local refinement of the design space allowed by the sequential learning method. The values of the global error estimates between the previous and present approaches are comparable, but the sequential method proved more computationally cost-effective. Further refinement in the optimal regions might be needed to improve predictive capability of surrogate models and to obtain the optimal solutions sets.

INTRODUCTION

Efficient fuel-air mixing, combustion, and flameholding are key fluid dynamic challenges for creating viable combustor flowpaths. Attempts to enhance the fuel-air mixing, while minimizing total pressure losses, thereby improving thrust potential, have received a great deal of attention over the years.[1] Although a certain amount of total pressure loss is expected due to the desired effect of molecular mixing of the fuel and air, further losses will reduce the thrust potential of the engine and should, therefore, be minimized.

Computational fluid dynamics (CFD) is currently widely used among researchers to explore and optimize fuel injection systems for aerospace applications. Among the available simulation tools, Reynolds-averaged simulation (RAS) is the most computationally efficient CFD method. However, even RAS can become prohibitively expensive when generating a dense database of objective function values for even a few design

---

variables. Therefore, Design and Analysis of Computer Experiments (DACE) methods are typically used to efficiently sample the design space in order to minimize the total cost of CFD simulations, fit surrogate models to approximate the objective function values away from the CFD simulations data, and utilize the resulting surrogate model to optimize the design.

Previously, multiobjective optimization of an interdigitated flushwall injector in a straight duct fueled by hydrogen was performed[2] by utilizing methods available in DAKOTA.[3] A database of objective function values was obtained by performing simulations using a Latin hypercube sampling (LHS) design, in addition to the corners of the hypercube of the design space. The number of RAS simulations in the LHS was guided by a) the minimum number of samples required to fit the relevant surrogate models and b) a guess of the total computational cost that the investigator would be willing to allocate. The optimization was carried out for several surrogate models, which were developed using databases of objective function values obtained from RAS. This approach exhibited relatively large predictive uncertainty near optimal design points (as high as 10%) due to the relatively large design space over which the surrogate models were fitted. The uncertainties could likely be reduced by continuing to augment the LHS with additional RAS, however, following this approach, it is not clear a priori how many more CFD simulations would be needed to obtain acceptable surrogate model fidelity.

In the present study, we reexamine the same problem while attempting to improve the surrogate model fidelity to predict optimal designs by using a sequential learning method.[4] The method relies on the same design space being sampled but with a goal to also minimize computational expense by allowing the subject matter expert to make sampling decisions based on currently available data in a sequential fashion. These decisions include whether further sampling is required and identifying which regions of the design space to sample. As before, surrogate models are used to approximate the objective function values and help guide the decision process. The downside of this approach is that it cannot be readily automated because user decisions are required during the sequential steps. However, at the same time, the user is forced to become familiar early in the analysis with the potential complexities of the design space, making the user better equipped at assessing the feasibility and correctness of the optimal solutions. DAKOTA and JMP[5] software were used to generate designs, perform parameter estimation, fit surrogate models, and perform optimization.

INJECTOR GEOMETRY AND FLOW CONDITIONS

The flushwall injector used in the current work introduces a number of flow features around the injection site that interact to produce a fluidic blockage. A bow shock forms upstream of the injection plume creating total pressure losses and aerodynamic blockage by forcing the air to flow around the fuel plume. The fuel plume entering the high-speed crossflow generates a counterrotating vortex pair, which becomes the main mechanism for stirring the fuel into the air. However, unlike a fuel placement device, such as a strut, the extent to which the fuel penetrates into the airflow is governed by fluidic considerations.[1,6–8] The jet penetration has been shown to be primarily proportional to the ratio of the orthogonal components of the dynamic pressure (or momentum flux) of the main air and the fuel jet, and is further enhanced by matching the static pressure at the exit of the fuel injector to the static pressure of the air just upstream of the fuel plume and downstream of the bow shock.

Top-down and side views and dimensional details of the flushwall injector geometry are shown in Fig.1. The port exit interface shape is derived from the multiobjective optimization work of Ogawa.[9] The injector port has a rectangular cross-section with the longer dimension aligned with the streamwise direction. Ogawa and Boyce[10] showed that a high aspect ratio rectangular cross-section port was desirable for high mixing efficiency and fuel penetration. More recently, Ogawa[9] showed that a high aspect ratio oval injector cross-section offers a slight improvement in mixing efficiency over a similar aspect ratio rectangular injector. The injection angle α, i.e., the angle of the port with respect to the streamwise direction, is variable and the port rotates about an axis coinciding with the intersection of the upstream port wall and the combustor plate as
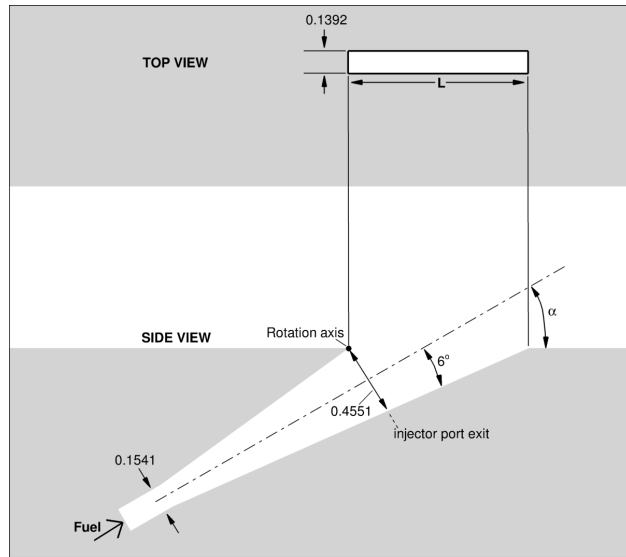
Figure 1. Dimensional details of the baseline flushwall injector (dimensions are in inches) (from Shenoy et al.[2]).

detailed in Fig.1. The injector also contains an expansion section with a 6 degree half-angle. The port width is fixed at 0.1392 inches and the throat height is 0.1541 inches. The expansion area ratio is approximately 2.95 at the exit height of 0.4551 inches. The area of the injector at the fuel exit plane varies with the injection angle. This area has length L of about 1.11 and 0.4551 inches at $\alpha = 30°$ and $90°$, respectively.

Figure 2 shows a schematic view of the flow cross section with its interdigitated arrangement of the flushwall injectors. An infinite row of interdigitated injectors is simulated. The duct height h is defined as the distance between the upper and lower combustor walls, while the spanwise spacing or width w is defined as the distance between two adjacent injector ports. The intended fueling area (IFA), denoted by dashed lines, is defined as the portion of the cross-sectional area of the duct that each injector is expected to fuel independently of the others. For the flushwall injector, an appropriate choice for the IFA is the half-height times the width ($h/2 \times w$).
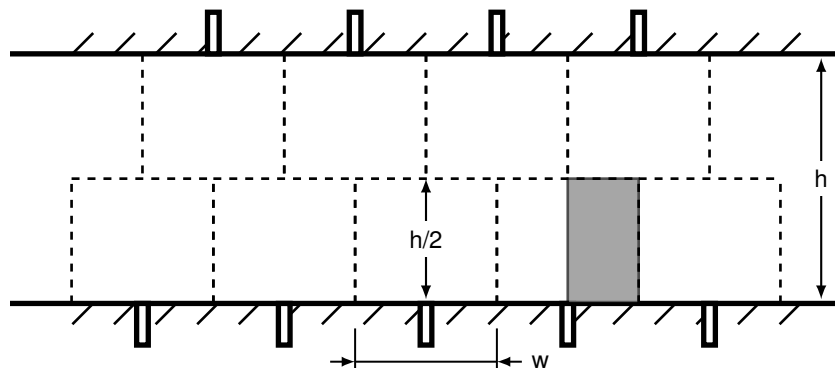

Figure 2. Schematic of the cross-section view of the ducted flowpath with a row of interdigitated flushwall injectors (from Shenoy et al.[2]). The region between dashed lines denote the IFA for each injector and the shaded area illustrates the cross-section of the computational domain used.

The flight trajectory of interest in this study takes the vehicle across a range of Mach numbers from 8 to 15 along a constant dynamic pressure trajectory of 1500 psf. To obtain the flow conditions at the flowpath entrance, the freestream air is compressed to 50.66 kPa with an inlet model assuming 95% isentropic efficiency and 99% adiabatic efficiency. The kinetic energy efficiency of this notional inlet is about 98%. The total inlet contraction ratio ranges from about 7.3 at a flight Mach number of 8 to about 20.0 at a flight Mach number of 15. Because the flowpath inflow area, defined by the product of the duct height and spanwise injector separation width, varies independently of the flight Mach number, the notional vehicle inlet capture area changes as a function of the flight Mach number. The combustor inflow Mach number ranges from about 3.7 to 6.4 as the flight Mach number increases. The freestream conditions for flight Mach numbers of 8 and 15 are shown in Table 1. A thermally perfect mixture of 21% oxygen (O_2) and 79% nitrogen (N_2) by volume was used for the air in the simulations. Hydrogen fuel is supplied at a total temperature of approximately 1200 K and its mass flow rate for each injector was computed based on an equivalence ratio (ER) of 0.75 over the IFA.

Table 1. Freestream conditions for the extrema of flight Mach numbers in the current simulations.

Alt. (km)	Mach No.	Q (kPa)	p (kPa)	T (K)	$T_0{}^\dagger$ (K)	$p_0{}^\dagger$ (MPa)
28.0	8.0	71.82	1.6048	232.4	2753.9	24.78
36.6	15.0	71.82	0.4565	249.4	8816.6	1333.2

†Value based on frozen composition of air

COMPUTATIONAL METHODOLOGY

The numerical simulations were performed using the Viscous Upwind aLgorithm for Complex flow ANalysis (VULCAN-CFD) code.[11] VULCAN-CFD is a cell-centered, finite-volume solver widely used for high-speed flow simulations. For this work, Reynolds-averaged simulations (RAS) were performed using structured, multiblock grids. The advective terms were computed using the Monotone Upstream-Centered Scheme for Conservation Laws (MUSCL) scheme[12] with the Edwards' Low-Dissipation Flux-Split Scheme (LDFSS).[13] The thermodynamic properties of the mixture components were computed using the curve fits of McBride et al.[14] The governing equations were integrated using an implicit diagonalized approximate factorization (DAF) method.[15] The current work used the Menter Baseline two-equation turbulence model.[16] The Reynolds heat and species mass fluxes were modeled using a gradient diffusion model with turbulent Prandtl and Schmidt numbers of 0.9 and 0.5, respectively. The chemical reactions were modeled using the nine-species / nineteen-reaction hydrogen air kinetic model of Ó Conaire et al.,[17] neglecting turbulence-chemistry interactions. Wilcox wall matching functions[18] were also used, however, their implementation in VULCAN-CFD includes a modification that allows the simulations to recover the integrate-to-the-wall behavior as the value of normalized wall-distance, y^+, approaches one. All simulations were converged until the total integrated mass flow rate and the total integrated heat flux on the walls remained constant to several significant figures. This typically occurred when the value of the L_2-norm of the steady-state equation-set residual decreased by about 3–4 orders of magnitude. To conserve the available computational resources, all the simulations were split into elliptic and space-marching regions. The elliptic region contained the inflow of the domain, the injector bodies, and up to 6.5 inches downstream of the injection plane. The computational cell count was about equal in both regions, but the computational cost associated with solving the space-marching region was about an order of magnitude lower than that for the elliptic region. Past simulation experience[19] with similar injector configurations have shown that this approach accurately simulates the flow as compared to using a single, fully elliptic region.

The computational domain is illustrated in Fig. 3. The inflow and outflow planes are placed at 9 inches upstream and 25 inches downstream, respectively, of the fuel injection plane located at X = 0. The left symmetry plane bisects the port and the right symmetry plane is located halfway between adjacent injector
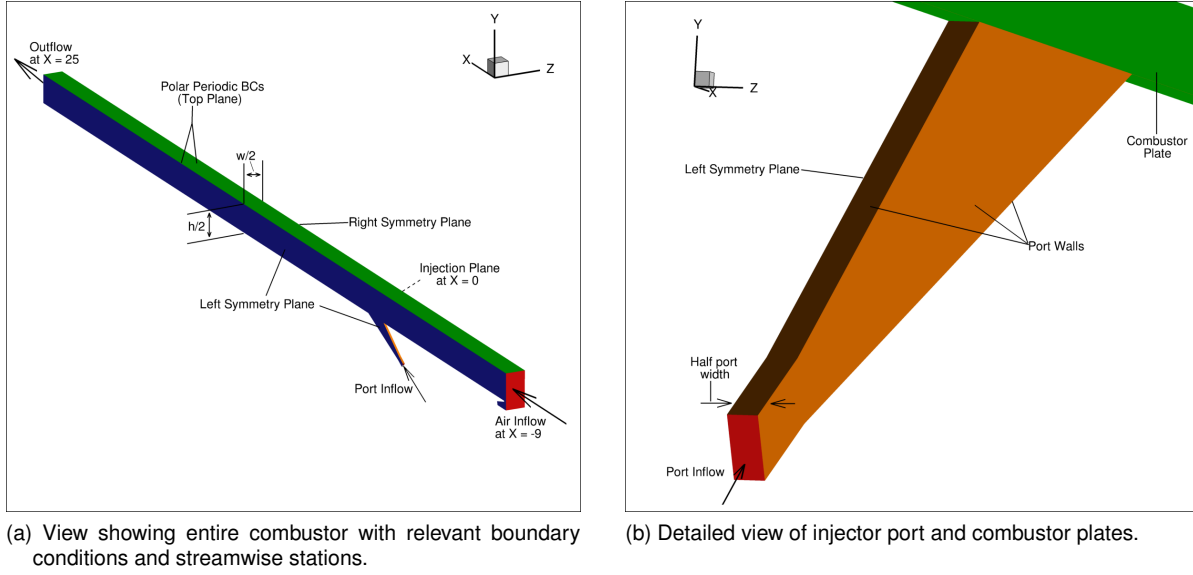
(a) View showing entire combustor with relevant boundary conditions and streamwise stations.

(b) Detailed view of injector port and combustor plates.

Figure 3. Computational domain of the combustor with relevant details (from Shenoy et al.[2]). All dimensions are in inches.

ports at a distance of $w/2$ from the left symmetry plane. The interdigitated symmetry is also leveraged by utilizing a pair of polar periodic boundary conditions on the top plane of the computational domain. The cross-sectional area of the computational domain corresponds to half the IFA and is shaded in gray in Fig. 2.

OBJECTIVE FUNCTIONS, DESIGN VARIABLES, AND GRID GENERATION

The performance of the fuel injection was evaluated using two metrics of interest. The first metric of interest is the thrust potential. This metric is obtained by expanding one-dimensional[20] values obtained from the simulations at each streamwise location through an ideal (isentropic) thrust nozzle. In the current work, this expansion process is evaluated until the flow reaches the static pressure at the combustor flowpath entrance. Another possibility would be to expand the flow to the freestream static pressure. The choice to expand the flow to the flowpath entrance static pressure is to limit the thrust potential values to those corresponding to the flowpath component only rather than the entire vehicle. The thrust potential is computed from:

$$TP = \dot{m}_e u_e + p_e A_e - \dot{m}_i u_i - p_i A_i \tag{1}$$

where TP is the stream thrust potential (not net thrust potential); $\dot{m}$, u, p, and A, are the mass flow rate, velocity, static pressure, and the area, respectively, with subscripts e and i denoting conditions at the thrust nozzle exit plane, and the flowpath entrance (inflow). Since the mass flow rate through the flowpath varies with the flight condition and the IFA, it is beneficial to normalize the thrust potential by the inflow mass flow rate to enable useful comparisons as the flight conditions change. The resulting mass-flow specific stream thrust potential is:

$$TP_m \equiv \frac{TP}{\dot{m}_i} = \frac{\dot{m}_e u_e + p_e A_e - p_i A_i}{\dot{m}_i} - u_i. \tag{2}$$

This metric represents an ideal potential mass-flow specific stream thrust that could be obtained when a flowpath of interest is truncated at a given streamwise location and coupled at that location to an ideal thrust nozzle. However, the flow in the thrust nozzle is assumed to be chemically "frozen" starting at the point of expansion, and therefore, this metric does not account for any additional mixing (thrust loss) and reaction

(thrust gain) during the expansion process. For the rest of this paper, this mass-flow specific stream thrust potential will be referred to as the thrust potential for brevity (TP_m). All of the total pressure losses still appear as a decrease in the value of the thrust potential, however, the total pressure losses due to chemical reactions, which energize the flow, could increase the value of the thrust potential.

The second metric of interest is the combustion efficiency, which quantifies how completely a given flowpath is able to process a mixture of fuel and air into combustion products, thereby enabling heat release into the flow. The combustion efficiency is selected in this work in addition to the thrust potential in order to incorporate designs that promote fuel mixing (and, thereby, combustion) as desirable, rather than designs that simply augment thrust via low-angle fuel injection. Because the equivalence ratio is less than one, the combustion efficiency is computed based on the depleted fuel mass flow rate, i.e.,

$$\eta_c = 1 - \frac{\dot{m}_f}{\dot{m}_{f,tot}} \tag{3}$$

where $\dot{m}_f$ and $\dot{m}_{f,tot}$ are the integrated mass flux of fuel at a streamwise location of interest and the total injected fuel mass flow rate, respectively.

Four parameters are used as design variables. These are the flight Mach number M, duct height h, width w, and the injection angle α. The bounds of these variables were chosen based on research interests and subject matter expertise guided by previous work. The optimization problem can be characterized as follows:

maximize: thrust potential: TP_m
combustion efficiency: η_c

subject to: Mach number: $8.0 \leq M \leq 15.0$
duct height: 1.0 in $\leq h \leq 3.0$ in
spanwise spacing (width): 0.8 in $\leq w \leq 2.0$ in
injection angle: $30° \leq \alpha \leq 90°$

Both optimization quantities are obtained at the exit of the domain, i.e., 25 inches downstream of the fuel injection plane. The flight Mach number bounds reflect the flight conditions of interest from previous work,[19] while the height and width bounds are selected based on estimates of where optimal solutions are expected. The injection angle bounds were selected based on the optimization effort of Ogawa.[9]

Simulation grids were generated using the GoHypersonic Inc. LINK3D software,[21] which enables efficient, parallel structured grid generation that is amenable to geometric modifications and design optimization. A methodology was developed that automatically generates the required geometry and performs grid smoothing and clustering based on the geometrical design parameters. First, using the geometric design variables, i.e., the height, width, and injection angle, geometry curves and surfaces are generated. Because the structured grid topology nodes reside in one-dimensional and two-dimensional coordinates with respect to their associated geometry curves and surfaces, respectively, the nodal locations can be automatically updated in response to a geometric modification. This allows for the same grid topology to be reused for any geometry in the design space. The second step involved assigning dimensions for a small group of edge families in the topology so that a nominal spacing of 0.01 inches was achieved. A computational grid dependence study was previously conducted by Drozda et al.[22] showing that this nominal spacing allows for numerical errors of approximately 5% in total pressure recovery and mixing efficiency. Finally, the structured grids, which ranged between 4.8 million cells to 23.8 million cells due to the expected variations in the flowpath geometry, were smoothed and clustered using LINK3D's parallel grid engine on a desktop machine, typically in one hour. Figure 4 shows slices of the grid at the left symmetry plane for two different geometric configurations. While the first case has a small injection angle and a large height, the second has a large injection angle and a smaller height.
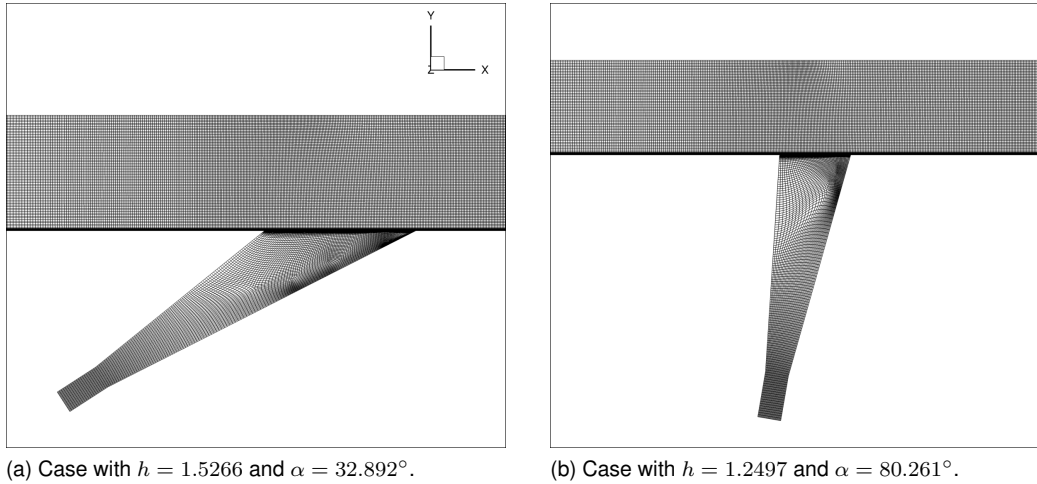
(a) Case with $h = 1.5266$ and $\alpha = 32.892°$.

(b) Case with $h = 1.2497$ and $\alpha = 80.261°$.

Figure 4. Grid slices at the port symmetry plane for two configurations (from Shenoy et al.[2]).

RESULTS AND DISCUSSION

The previous study sampled the design space efficiently using DAKOTA's LHS.[3] LHS is a DACE method that generates space-filling samples over a multidimensional design space. Previously, fifty samples were chosen to cover the entire design space over the four design variables. Additionally, sixteen corner points of the four-variable hypercube were also chosen to anchor the surrogate models and improve accuracy near the corners. This fifty-point LHS design set is labeled *LHS-50*, while the union of this set and the corners is labeled *LHSFF-66*. The current study, which uses the sequential learning method, leverages some of these solutions either as part of a new design set for training or as part of a validation set. For the rest of this paper, the terms "design" and "design sets" are used interchangeably specifically to refer to the sampling design methology.

Full Factorial with Center Point Design Sampling Methodology (*FFCP-17*)

The first sequential design chosen was a two-level factorial design augmented by the center point of the design space, resulting in a total of 17 points and labeled *FFCP-17*. The sixteen corner points of the four-variable hypercube performed previously[2] were reused here, with only one new simulation performed for the center point (the point with midpoint values for each design variables). This design supports a surrogate model that can account for the main-effects and two-factor interactions (a 2nd-order polynomial with no square terms of the variables) and has the ability to detect curvature. *FFCP-17* additionally enables an efficient initial exploration with the ability to screen less important variables out of the design. JMP[5] software is used here to examine the raw data via scatter plots, fit and visualize response surfaces, and perform parameter estimation in order to screen the design variables. Scatter plots of all four design variables and the resulting objective functions are plotted in Fig. 5 (a). The thrust potential shows little variation for designs with low Mach number and high height, and significant variation for designs with high Mach number and low height, suggesting that Mach number and height are significant parameters for these objective functions. The highest thrust potentials (values near 300 m/s) occur when both the Mach number and height are high. However, the combustion efficiency is poor for these cases (< 0.50). There are a number of designs that yield thrust potential values near 200 m/s with combustion efficiency varying between 0.50 and 0.95. Among these designs, four have high combustion efficiency (> 0.90), occurring at the low Mach number and low height values. Response surface fits for the two objective functions are plotted in Figs. 5 (b) and (c) for fixed values of width (2 in) and injection angle (60°). It can be observed that the region of high Mach number
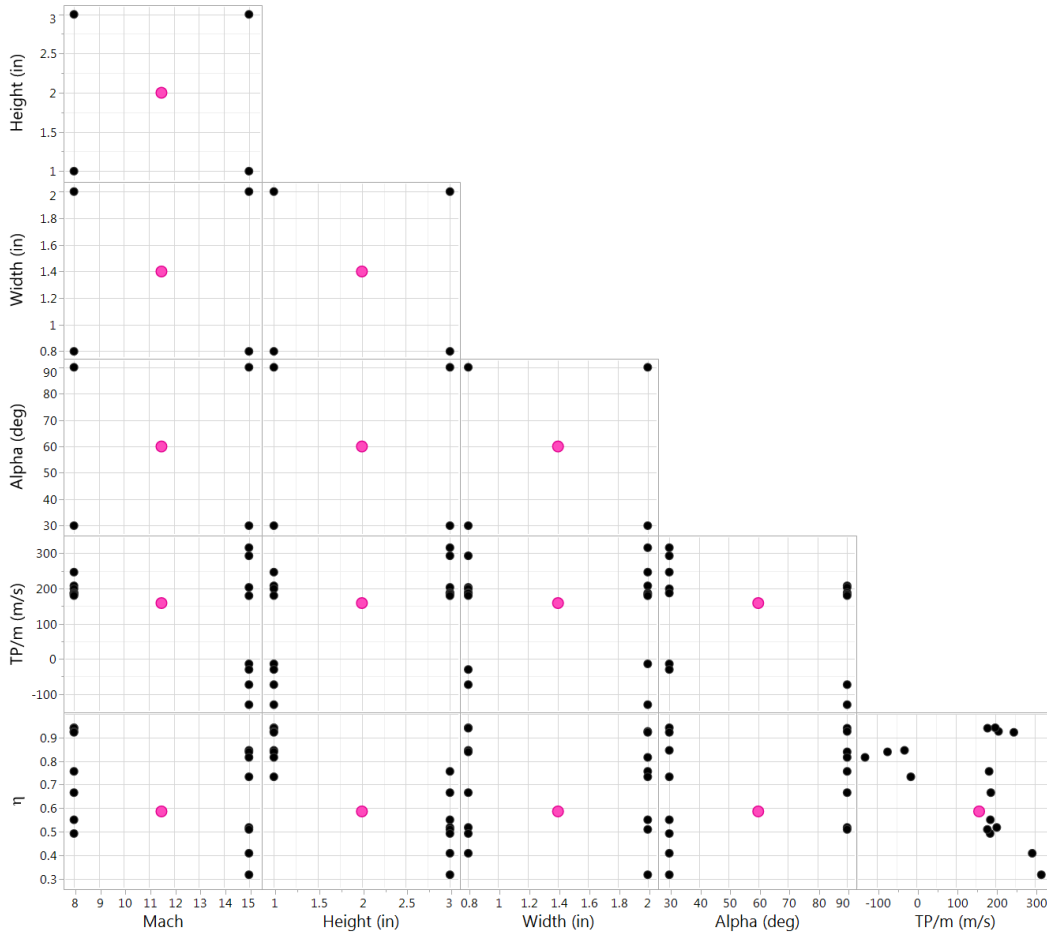
(a) Scatter plots
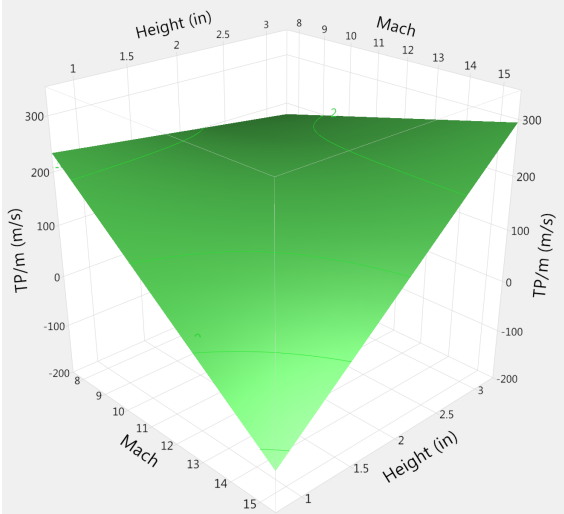
(b) TP_m v. M and h ($w = 2.0$ in, $\alpha = 60°$).
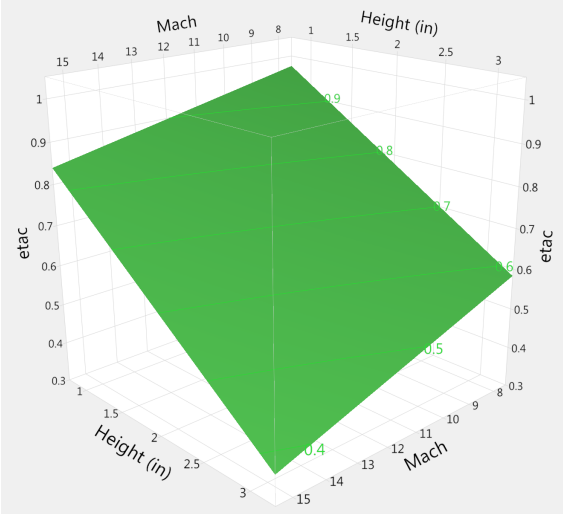
(c) η_c v. M and h ($w = 2.0$ in, $\alpha = 60°$)

Figure 5. Scatter plots and response surface fits for the *FFCP-17* design.

and high height yields high thrust potential but moderate to low combustion efficiency. The region where both Mach number and height are low exhibits high values for both thrust and combustion efficiency. The center point residuals were not small (approximately -12 m/s for thrust potential and 0.11 for combustion efficiency), indicating that a 2nd-order response surface capturing additional response curvature could be beneficial. Table 2 lists the parameter estimate outputs for both objective functions sorted by the magnitude of the terms. The variable bounds are coded or scaled between -1 and +1 so that the magnitude of the coefficients or estimates are comparable between each other. The most influential parameters for the thrust potential response (with estimates > 10 m/s) are Mh, h, M, α, and $M\alpha$, while those for the combustion efficiency (estimates > 0.03) are h, M, α, and $h\alpha$. These parameters show that the width is not as influential as the other parameters for either objective over the full design space.
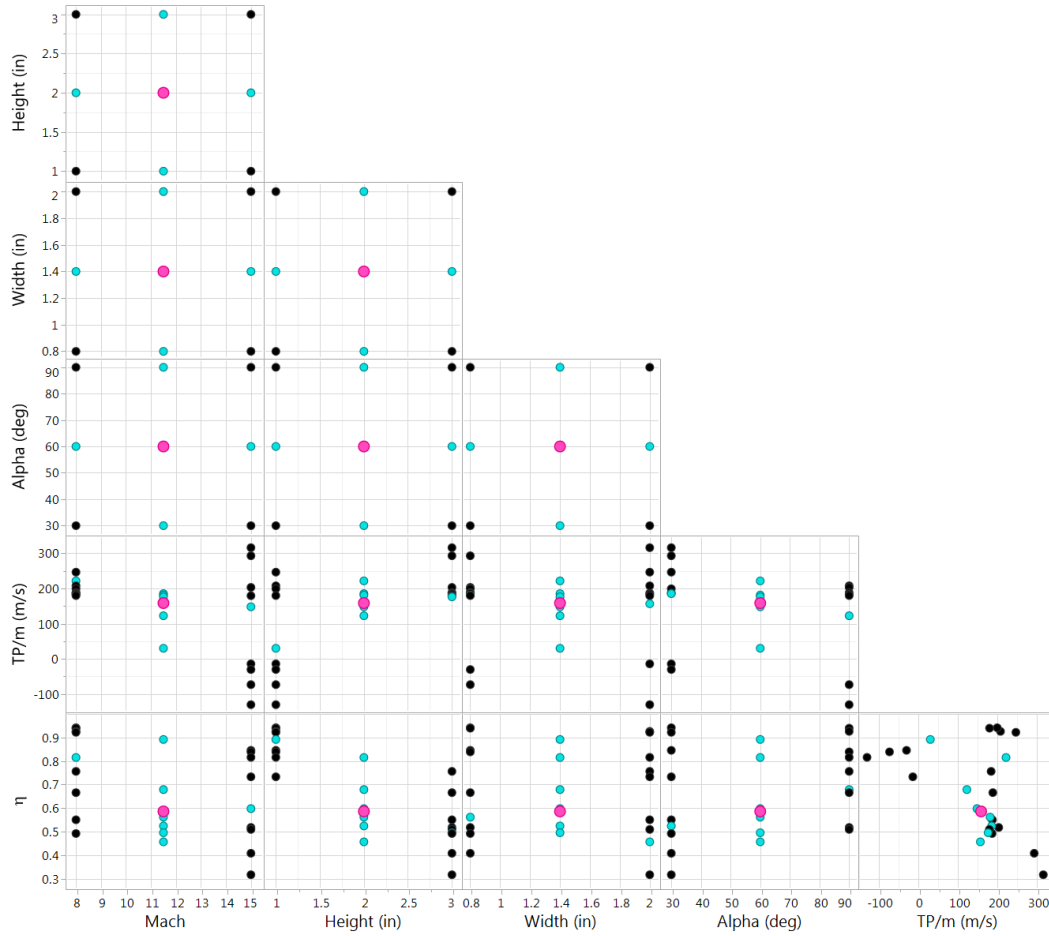
Table 2. Coded variable estimates ranked for both objective functions for the *FFCP-17* design.

| TP_m		η_c	
Term	Estimate	Term	Estimate
Intercept	146.262	Intercept	0.69246
$M_c \times h_c$	82.975	h_c	-0.17169
h_c	72.004	M_c	-0.07553
M_c	-52.210	α_c	0.04749
α_c	-27.809	$h_c \times \alpha_c$	0.03773
$M_c \times \alpha_c$	-20.364	$M_c \times w_c$	-0.02194
$w_c \times \alpha_c$	-9.004	$h_c \times w_c$	0.01362
$M_c \times w_c$	-7.055	$M_c \times h_c$	-0.01351
$h_c \times w_c$	-2.401	$w_c \times \alpha_c$	0.01313
w_c	1.845	w_c	-0.00748
$h_c \times \alpha_c$	-0.658	$M_c \times \alpha_c$	-0.00019

Face Centered Central Composite Design Sampling Methodology (*FCCCD-25*)

In order to obtain a full 2nd-order response surface, additional design points were simulated at the eight axial points or face-centers of the four-dimensional hypercube, i.e., the set of design points where one variable is at an extremum, while the other variables are at their midpoints. The *FFCP-17* design was augmented with these eight axial points to produce a 25-point design, which is a face centered central composite design,[23] labeled *FCCCD-25*. The teal colored points in the scatter plots in Fig. 6 (a) illustrate the axial points of this design. The low Mach number axial point has a thrust potential and combustion efficiency of approximately 220 m/s and 0.82, respectively, while the low height axial point has a thrust potential and combustion efficiency of approximately 50 m/s and 0.90, respectively. Figures 6 (b) and (c), when compared against their counterparts for the *FFCP-17* design (Fig. 5) show that quadratic terms in both the Mach number and height appear significant. This is confirmed from the parameter estimates listed in Table 3, where for the thrust potential, h^2 and M^2 appear significant (in addition to the same set of parameters that were shown to be important using the main-effects and two-factor interaction models), and for the combustion efficiency, M^2, w^2, and h^2 are now also important.

At this point, upon examining the outputs of the objectives over the design space, two regions of the design space were identified for further study. The first region is identified as the high Mach number, high height, and low injection angle region. It is bound approximately between the Mach numbers of 13 and 15, heights of 2 to 3, and injection angle of 30 to 60 degrees. Since width is not identified as a main-effect parameter, its value is kept constant with $w = 2.0$ because it yielded slightly higher thrust potential. This region allows for a high thrust potential design at the expense of combustion efficiency, which is desirable if thrust potential is significantly more important than the combustion efficiency. Such a situation would arise when a design yields low total pressure losses or low drag. The second region is identified as the low Mach number and low height region. It is bound approximately between the Mach numbers of 8 and 10, and heights of

(a) Scatter plots
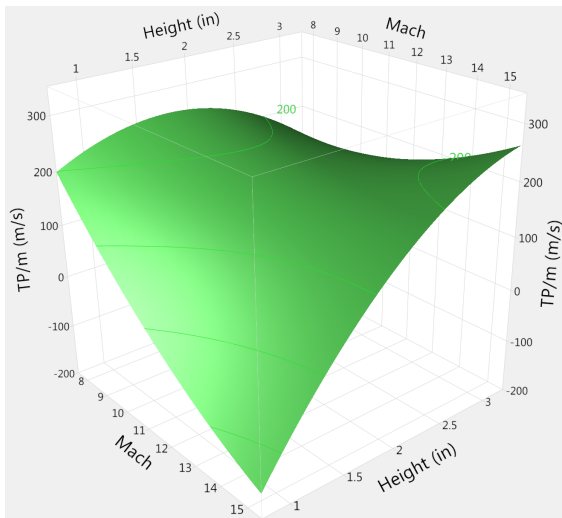
(b) TP_m v. M and h ($w = 2.0$ in, $\alpha = 60°$).
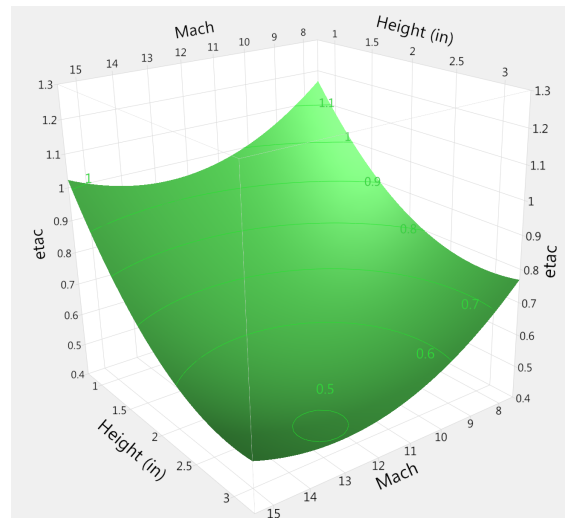
(c) η_c v. M and h ($w = 2.0$ in, $\alpha = 60°$)

Figure 6. Scatter plots and response surface fits for the *FCCCD-25* design.

Table 3. Coded variable estimates ranked for both objective functions for the *FCCCD-25* design.

| TP_m		η_c	
Term	Estimate	Term	Estimate
Intercept	156.184	Intercept	0.60097
$M_c \times h_c$	82.975	h_c	-0.17463
h_c	72.131	M_c^2	0.10345
h_c^2	-52.250	w_c^2	-0.09401
M_c	-50.496	h_c^2	0.09055
M_c^2	29.399	M_c	-0.07922
α_c	-28.214	α_c	0.05081
$M_c \times \alpha_c$	-20.364	$h_c \times \alpha_c$	0.03773
w_c^2	13.581	$M_c \times w_c$	-0.02194
$w_c \times \alpha_c$	-9.004	$h_c \times w_c$	0.01362
$M_c \times w_c$	-7.055	$M_c \times h_c$	-0.01351
$h_c \times w_c$	-2.401	$w_c \times \alpha_c$	0.01313
α_c^2	-1.497	w_c	-0.01248
$h_c \times \alpha_c$	-0.658	α_c^2	-0.00157
w_c	0.271	$M_c \times \alpha_c$	-0.00019

1 to 2. There is no preference for the injection angle as both the high and lower injection angles provide comparable values for both objective functions. The width value is set to $w = 2.0$ because it yielded a higher thrust potential design. This region allows for a relatively high thrust potential and high combustion efficiency design. For such designs, the high heat release due to high combustion efficiency would contribute to high thrust potential, that would overcome the thrust potential loss due to low total pressure recovery.

Face Centered Central Composite with Local Box-Behnken Design Sampling Methodology (*FCCCD+2BB-51*)

Since the extents of the two subregions vary as a function of only three variable factors (w is kept constant), local Box-Behnken designs[24] are appropriate for local refinement. This results in thirteen new simulation points for each subregion. Adding these new designs to the *FCCCD-25* design, results in a 51-point design set, labeled *FCCCD+2BB-51*. Figures 7 and 8 show the Mach number contours in order to highlight the differences in the physics occurring within the low Mach number and high Mach number regions, respectively. The black isolines denote the stoichiometric value of the fuel mass fraction. The small duct height, in conjunction with the normal injection angle for the low Mach number design (Fig. 7), results in lower thrust potential due to high total pressure losses that result from the shock reflections and greater combustion efficiency as the fuel is mixed into the flow well ahead of the exit of the combustor. The high Mach number design (Fig. 8) yields a high thrust potential by opening up the duct, which reduces the total pressure losses that occur from the shock reflections, as well as the low injection angle that augments the momentum in the streamwise direction. However, since the fuel does not penetrate into the airstream and because there is unmixed fuel at the exit of the combustor, a low combustion efficiency is obtained. One-dimensional combustor performance plots of the thrust potential and combustion efficiency are plotted for these two designs in Fig. 9. The low Mach number design shows the thrust potential initially decreasing due to the prevalence of total pressure losses but increases after around $X = 5$ in as the high combustion efficiency provides enough heat release to overcome these losses. When the combustion efficiency starts to plateau at around $X = 15$ in, the thrust potential also reaches its peak and then decreases due to further total pressure losses. The high Mach number design shows that the thrust potential is at its maximum immediately after injection and then monotonically decreases as the combustion efficiency monotonically increases with a lower slope than that of the low Mach number design.
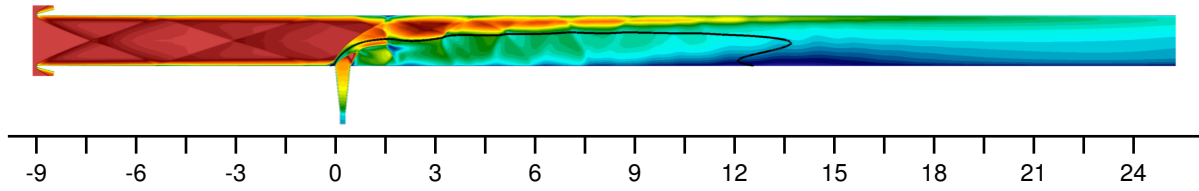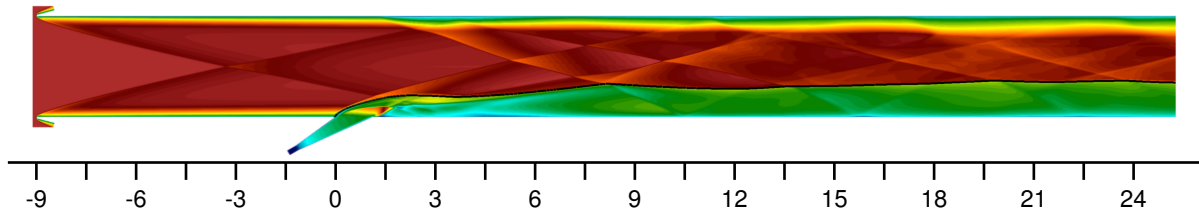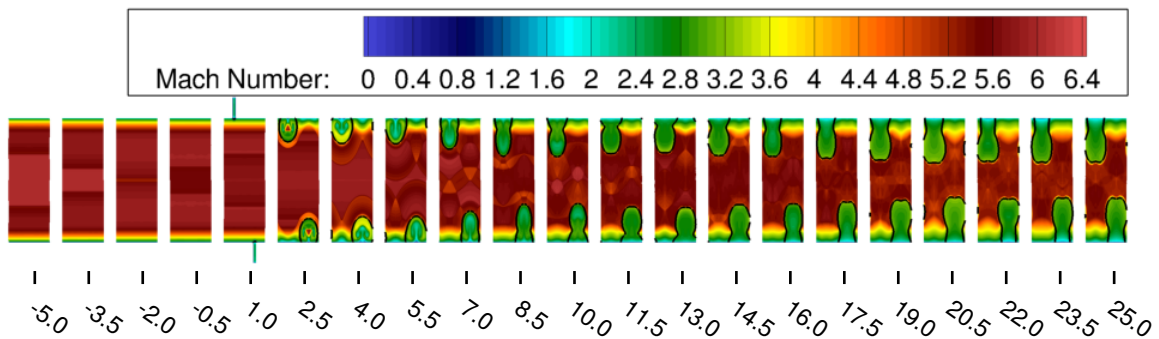
(a) Side view of the port symmetry plane.
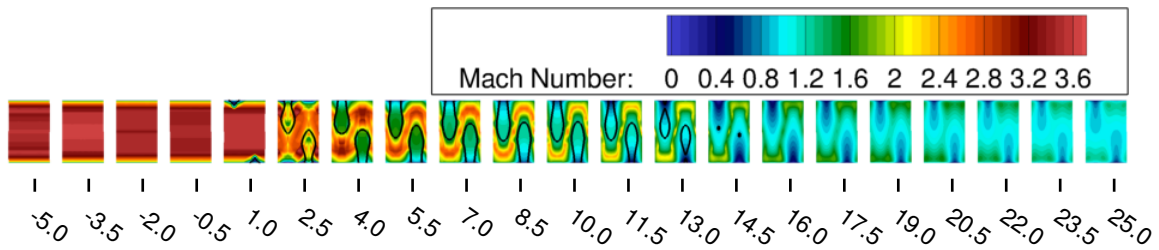
(b) Cross-stream planes.

Figure 7. Mach contours with black isolines denoting stoichiometric value of the fuel mass fraction for $M = 8.0$, $h = 1.5$, $w = 2.0$, $\alpha = 90°$**.**

(a) Side view of the port symmetry plane.

(b) Cross-stream planes.

Figure 8. Mach contours with black isolines denoting stoichiometric value of the fuel mass fraction for $M = 14.0$, $h = 3.0$, $w = 2.0$, $\alpha = 30°$**.**

(a) Case with $M = 8.0$, $h = 1.5$, $w = 2.0$, $\alpha = 90°$.   (b) Case with $M = 14.0$, $h = 3.0$, $w = 2.0$, $\alpha = 30°$.
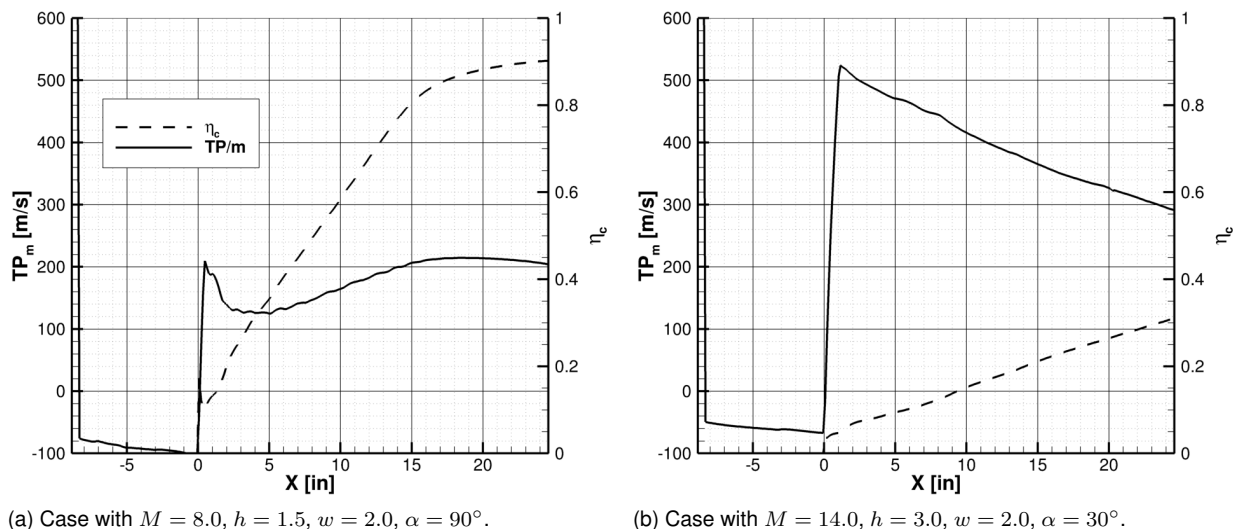
Figure 9. One-dimensional performance plots of thrust potential and combustion efficiency for design points within the (a) low and (b) high Mach number local BB designs.

The green points in the updated scatter plot (Fig. 10 (a)) highlight the new simulations resulting from the two Box-Behnken design sets. For both subregions of interest, there are a few new points that are near the optima, where for the high Mach number region high thrust potential is achieved, and for the low Mach number region high combustion efficiency with relatively high thrust potential is obtained. Using a Gaussian process (GP) spatial-interpolation model, all the training design points are fitted such that zero residual error is obtained with respect to these training data. For regions in between training points, the model serves as an interpolant, with its uncertainty decreasing near the training design points. The GP model surface plots (Figs. 10 (b) and (c)) for this design show more ripples, ridges, and troughs on the surface when compared against the second-order response surface fits for the *FCCCD-25* design, indicating that portions of the design space are feature rich and may not be adequately modeled with a second-order response surface. The GP surfaces indicate that near $M = 8.0$ at heights less than 1.5 in, thrust potentials exceed 200 m/s while obtaining combustion efficiency values greater than 80%. The highest thrust potentials are obtained for designs close to $M = 15.0$ for heights near 3.0 in, where combustion efficiency is poor.

Multiobjective design optimization is performed using the GP model using DAKOTA's multiobjective genetic algorithm. The algorithm starts with a randomly generated population over the design space using the surrogate model, instead of RAS, to obtain objective function responses. The best design points are then allowed to survive over several generations by performing crossover and mutation operations, and assessing the fitness of each member in the population. The algorithm is terminated when a convergence criterion is met. In this effort, an LHS population is generated for optimization with 500 initial points. This initial number was determined from a population size sensitivity study. Reproduction requires that two parents generate two offspring and the crossover and mutation rates are set to 0.8 and 0.1, respectively. These values are selected based on best-practice recommendations and parameters chosen by Ogawa.[9] Optimization using the current GP model with local design space refinement from the *FCCCD+2BB-51* design is compared against the previously obtained GP model using LHS[19] with 66 points (*LHSFF-66*).

Figure 11 shows the final populations of nondominated solutions obtained using GP models fitted to the *FCCCD+2BB-51* and *LHSFF-66* design sets, denoted by circle and square symbols, respectively. For the two objective functions, TP_m and η_c, a nondominated solution means that no further improvement of one function was found without a tradeoff from the other function. The set of these nondominated solutions obtained from each model is also known as a Pareto Front (PF). These sets are connected by black lines,

(a) Scatter plots
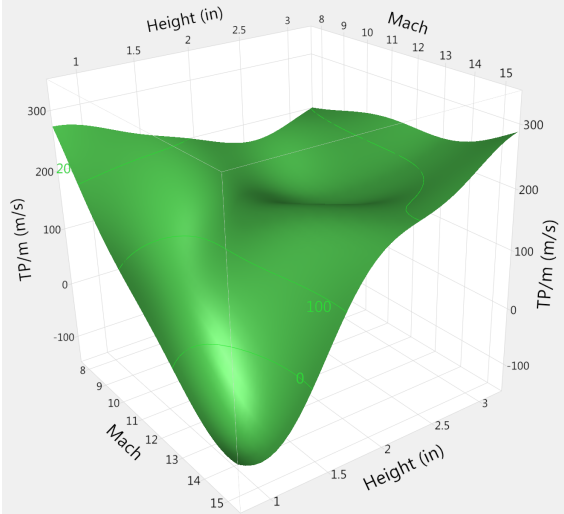
(b) TP_m v. M and h ($w = 2.0$ in, $\alpha = 60°$).
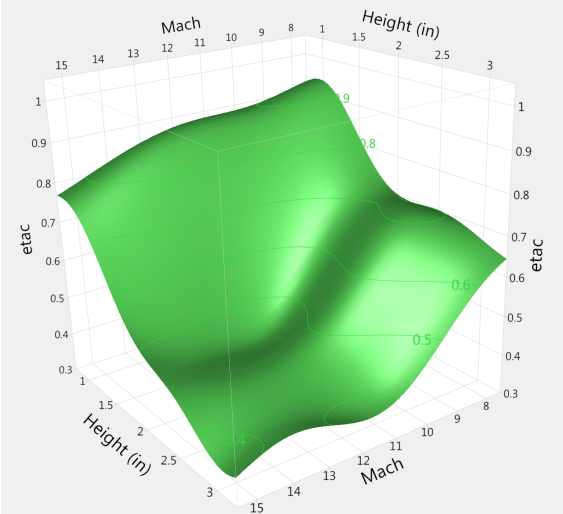
(c) η_c v. M and h ($w = 2.0$ in, $\alpha = 60°$)

Figure 10. Scatter plots and GP model surface for the *FCCCD+2BB-51* design.

highlighting discontinuities in the PFs. The plots also show the two training design sets in open symbols (squares for *FCCCD+2BB-51* and circles for *LHSFF-66*), with their common design points (the corners of the hypercube) in open diamond symbols. Additionally, the PF and training solutions are colored by the different design variables in each of the subplots, illustrating the effect of changes in the design variables. The PF resulting from the GP model trained by the *LHSFF-66* set only occurs at Mach numbers of about 8 where the combustion efficiency is greater than 0.85. This PF exhibits a discontinuity between solutions where height is 1.0 in, where thrust potential is lower, and those where the height is around 1.5 in where thrust potential is higher. The PF resulting from the GP model trained by the *FCCCD+2BB-51* set occurs at Mach numbers of about 8 for heights between 1.0 in and 2.0 in and Mach numbers of about 15 for a height of about 3.0 in. A small subset of this PF shows combustion efficiency values greater than 1, which represents an extrapolation error, because the GP model is only constrained by the physics at the training points. Comparing the PFs for combustion efficiency around 0.90, there is a higher prediction of the thrust potential from the *LHSFF-66* design set by approximately 30–40 m/s. The differences between these PFs are attributable to the GP model's increase in uncertainty for points significantly away from the training data. The *LHSFF-66* design only has two training points (corners) where thrust potential is high and combustion efficiency is low (at Mach 15, height of 3.0 in, and injection angle at 30°), while the *FCCCD+2BB-51* design has five training points (due to the local Box-Behnken refinement) in the same region. Therefore, there is more uncertainty in the GP model obtained by the *LHSFF-66* design in the high Mach number region, and the sequential addition of the Box-Behnken local designs leads to locally improved prediction of optimal solutions.

The global accuracy of the models is assessed using two methods: leave-one-out cross-validation (LOO-CV) and using a set of challenge points. The LOO-CV is computed using only data available within the training set, so that no additional challenge points are required to compute an error metric. For a training set with N points, one point is left out and the remaining $N-1$ points are used to compute a model, which is evaluated at the point left out. This process is repeated until all N points are left out and N models are available, with the root-mean-squared (RMS) error for each model computed with respect to the left out point. The challenge point set involves evaluating the surrogate model at points that the model was not trained on. For the new design sets discussed in this paper (*FCCCD-25* and *FCCCD+2BB-51*) the challenge set comprised the *LHS-50* set and three additional challenge points that were already available from the previous study of Shenoy et al.[2] Additionally, in order to evaluate the quadratic response surface (RS) and GP models trained using the *LHSFF-66* set from the previous study,[2] the 35 unique points from the *FCCCD+2BB-51* set (16 corners omitted) and the three additional challenge points serve as the challenge set. The RMS error estimates computed using both these methods for the different models trained using the different designs are shown in Table 4. The LOO-CV errors are comparable between the quadratic RS models resulting from the *FCCCD-25* and *LHSFF-66* designs, but the challenge set errors show lower error for the combustion efficiency (-0.02 η_c) for the *LHSFF-66* set. However, this training set represents computational cost of more than 2.5 times that of the *FCCCD-25* set. Comparing the LOO-CV errors from the GP models resulting from the *FCCCD+2BB-51* and *LHSFF-66* sets showed that the thrust potential error is comparable, but combustion efficiency error reduces (-0.02 η_c) for the *FCCCD+2BB-51* set. However, using the challenge sets, the errors for both the thrust potential and combustion efficiency are lower for the *LHSFF-66* set. Since the errors are overall not substantially lower using the *LHSFF-66* set, the LHS was not as cost-effective as the current design set that was arrived at using a sequential learning method.

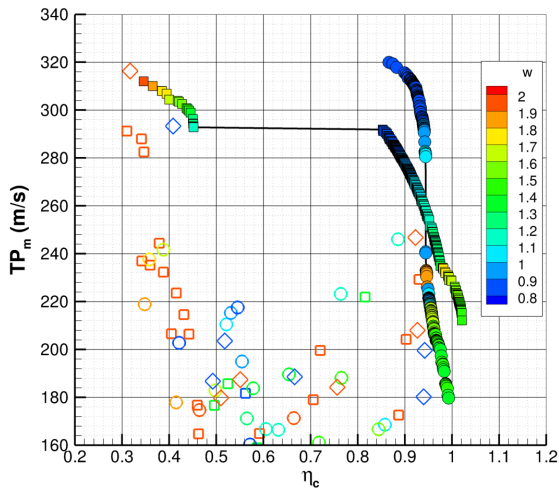**Table 4. RMS errors for the different models trained using the different designs.**

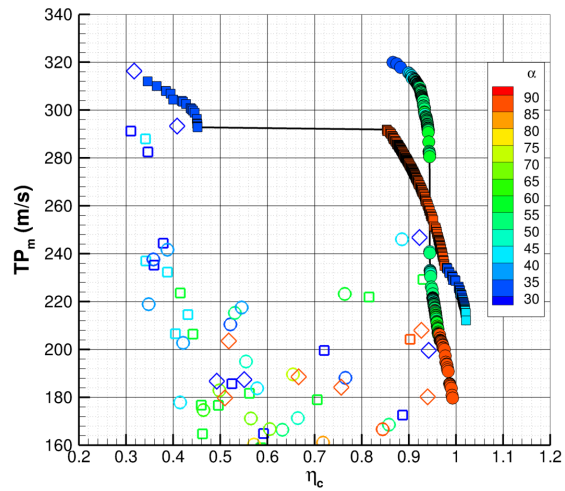|		*FCCCD-25* (RS)	*LHSFF-66* (RS)	*FCCCD+2BB-51* (GP)	*LHSFF-66* (GP)
TP_m	LOO-CV	32.2	29.8	24.7	23.9
(m/s)	Challenge Set	28.5	30.0	28.8	20.7
η_c	LOO-CV	0.056	0.056	0.037	0.056
	Challenge Set	0.065	0.045	0.058	0.045
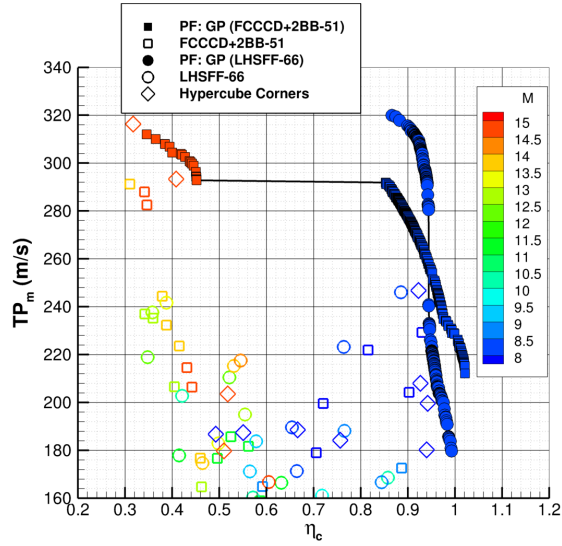
(a) Solutions with symbols colored by Mach number.
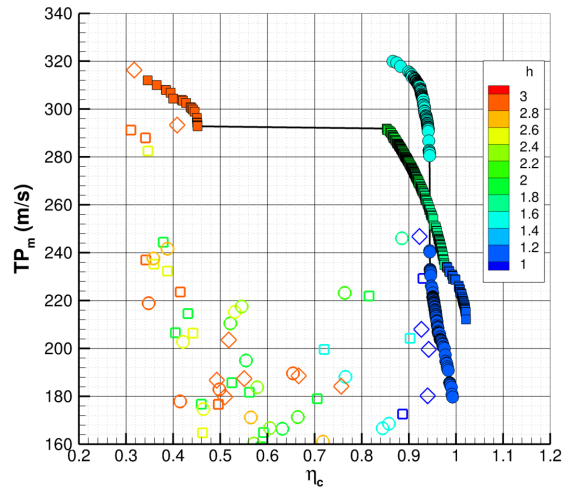
(b) Solutions with symbols colored by height.

(c) Solutions with symbols colored by width.

(d) Solutions with symbols colored by injection angle.

Figure 11. Optimization solutions using GP model trained with *FCCCD+2BB-51* design compared against the GP model trained with previous *LHSFF-66* set.

It is important to note that these global error estimates represent the predictive capability of these surrogate models over the entire design space, rather than in the regions of optima. By examining the errors of the GP model trained by the *FCCCD+2BB-51* design set obtained using the subset of challenge points that reside within the local refinement regions, the thrust potential error reduces to 17.9 m/s (compared to 28.8 m/s for the entire challenge set) and the combustion efficiency error increases to 0.069 (compared to 0.058). The combustion efficiency error levels are comparable with the numerical errors due to grid dependence of about 5%.[22] In order to further reduce the level of error around predicted optima, it may be desirable to introduce additional refinement of the design space along the PF. New design points along last predicted optima may then be used to obtain updated error estimates for the current iteration's GP model prior to using them as additional training data for the subsequent iteration.

SUMMARY AND CONCLUSIONS

A numerical investigation was conducted in order to demonstrate the use of DACE methods in DAKOTA and JMP via a sequential learning approach to surrogate modeling and optimization. These methods were applied to a combustor flowpath fueled with an interdigitated flushwall injector and ascending along a constant dynamic pressure flight trajectory. The flight Mach number, duct height, spanwise spacing, and injection angle were the design variables for optimizing thrust potential and the combustion efficiency of the flowpath. Because RAS is computationally expensive, surrogate models that accurately capture the RAS-derived objective functions were desired in order to identify optimal regions of the design space and assess if these models can provide accurate predictive capability. This effort leveraged results obtained in a previous effort,[2] which studied the same optimization problem, but used an LHS design with an a priori picked sample size based on computational constraints. The present work, on the other hand, used a sequential learning method that enables the investigator to cheaply screen the design space and learn about the objective function responses, and progressively identify local regions of interest for further analysis. The first step involved the use of a main-effects with two-factor interaction model that identified that the width was not as important over the design space as the other design variables, and that the design space exhibited uncaptured curvature. The next step added new design points to support a full second-order response surface model capable of capturing the design space curvature. Analysis of this new model by visualizing the objective functions helped identify two subregions of interest: one near the low Mach number limit and the other near the high Mach number limit. These subregions were further populated using Box-Behnken designs, yielding a new 51-point design set. To take full advantage of the local refinement of the design space, and bring about any local features, a GP model was fitted to this design set and optimization was performed using a multiobjective genetic algorithm. The comparisons of the PF obtained from the previous and current efforts revealed differences that were attributed to the differences in the density of training data in the vicinity of the optima. The global error estimates were comparable between the models obtained previously and from the current efforts. Because the current effort involved fewer RAS, the sequential learning method appears more computationally cost-effective as compared to the LHS. However, the predictive capability in optimal regions may need to be further enhanced by performing additional refinement near the optima and iteratively reducing the local errors.

ACKNOWLEDGMENTS

REFERENCES

[1] Lee, J., Lin, K.-C., and Eklund, D., ***Challenges in Fuel Injection for High-Speed Propulsion Systems***, AIAA J., 53(6):1405–1423 (Jun. 2015).

[2] Shenoy, R. R., Drozda, T. G., Axdahl, E. L., and Baurle, R. A., ***Numerical Investigation and Optimization of a Flushwall Injector for Scramjet Applications at Hypervelocity Flow Conditions***, in *JANNAF Meeting / 49th CS / 37th APS / 37th EPSS / 31st PSHS Joint Subcommittee Meeting*, NTRS Report Number NF1676L-31988, Dayton, OH (Jun. 2019).

[3] Adams, B., Ebeida, M., Eldred, M., Geraci, G., Jakeman, J., Maupin, K., Monschke, J., Stephens, J., Swiler, L., Vigil, D., Wildey, T., Bohnhoff, W., Dalbey, K., Eddy, J., Frye, J., Hooper, R., Hu, K., Hough, P., Khalil, M., Ridgway, E., Winokur, J., and Rushdi, A., ***DAKOTA, A Multilevel Parallel Object-Oriented Framework for Design Optimization, Parameter Estimation, Uncertainty Quantification, and***

Sensitivity Analysis: Version 6.8 User's Manual, Sandia Technical Report SAND2014-4633, Sandia (May 2018).

[4] Box, G. E. P., ***Statistics as a Catalyst to Learning by Scientific Method Part II – A Discussion***, Journal of Quality Technology, 31(1):16–29 (1999).

[5] ***JMP***, Version 13.2, SAS Institute Inc., Cary, NC (1989–2019).

[6] Schetz, J. A. and Billig, F. S., ***Penetration of Gaseous Jets Injected into a Supersonic Stream***, J. Spacecraft. Rockets., 3(11):1658–1665 (1966).

[7] Mao, M., Riggins, D. W., and McClinton, C. R., ***Numerical Simulation of Transverse Fuel Injection***, in *Computational Fluid Dynamics Symposium on Aeropropulsion*, NASA-CP-3078, pages 635–667, NASA, Cleveland, OH (Apr. 1990).

[8] Portz, R. and Segal, C., ***Penetration of Gaseous Jets in Supersonic Flows***, AIAA J., 44(10):2426–2429 (Oct. 2006).

[9] Ogawa, H., ***Physical Insight into Fuel-Air Mixing for Upstream-Fuel-Injected Scramjets via Multi-Objective Design Optimization***, J. Propul. Power., 31(6):1505–1523 (2015).

[10] Ogawa, H. and Boyce, R. R., ***Multi-Objective Design Optimization of Fuel Injection for Mixing Enhancement in Scramjets by Using Surrogate-Assisted Evolutionary Algorithms***, in *18th AIAA/3AF International Space Planes and Hypersonic Systems and Technologies Conference*, Tours, France (Sep. 2012).

[11] VULCAN-CFD, ***http://vulcan-cfd.larc.nasa.gov/*** (Dec. 2017).

[12] van Leer, B., ***Towards the Ultimate Conservative Difference Scheme. V: A Second-Order Sequel to Godunov's Method***, J. Comput. Phys., 32(1):101–136 (Jul. 1979).

[13] Edwards, J. R., ***A Low-Diffusion Flux-Splitting Scheme for Navier-Stokes Calculations***, Comput. Fluids., 26(6):635–659 (Jul. 1997).

[14] McBride, B. J., Gordon, S., and Reno, M. A., ***Thermodynamic Data for Fifty Reference Elements***, NASA Technical Paper 3287/REV1, NASA, Cleveland, OH (Feb. 2001).

[15] Pulliam, T. H. and Chaussee, D. S., ***A Diagonal Form of an Implicit Approximate-Factorization Algorithm***, J. Comput. Phys., 39(2):347–363 (Feb. 1981).

[16] Menter, F. R., ***Two-Equation Eddy-Viscosity Turbulence Models for Engineering Applications***, AIAA J., 32(8):1598–1605 (Aug. 1994).

[17] Ó Conaire, M., Curran, H. J., Simmie, J. M., Pitz, W. J., and Westbrook, C., ***A Comprehensive Modeling Study of Hydrogen Oxidation***, Int. J. Chem. Kinet., 36(11):603–622 (2004).

[18] Wilcox, D. C., ***Turbulence Modeling for CFD***, DCW Industries, Inc., La Cañada, CA (2000).

[19] Shenoy, R. R., Drozda, T. G., Norris, A. T., Baurle, R. A., and Drummond, J. P., ***Comparison of Mixing Characteristics for Several Fuel Injectors at Mach 8, 12, and 15 Hypervelocity Flow Conditions***, in *AIAA Propulsion and Energy Forum*, Cincinnati, OH (Jul. 2018).

[20] Baurle, R. and Gaffney, R., ***Extraction of One-Dimensional Flow Properties From Multidimensional Data Sets***, J. Propul. Power., 24(4):704–714 (Aug. 2008).

[21] Drayna, T., Haag, C., Bartkowicz, M., and Gidzak, V., ***LINK3D***, Software package, version 1.0.0, GoHypersonic, Inc. (2016).

[22] Drozda, T. G., Drummond, J. P., and Baurle, R. A., ***CFD Analysis of Mixing Characteristics of Several Fuel Injectors at Hypervelocity Flow Conditions***, in *52nd AIAA/SAE/ASEE Joint Propulsion Conference*, AIAA 2016-4764, AIAA, Salt Lake City, UT (Jul. 2016).

[23] Box, G. E. P. and Wilson, K. B., ***On the Experimental Attainment of Optimum Conditions***, Journal of the Royal Statistical Society, Series B., 13(1):1–45 (1951).

[24] Box, G. E. P. and Behnken, D. W., ***Some New Three Level Designs for the Study of Quantitative Variables***, Technometrics, 2(4):455–475 (1960).